Chemical Science

ROYAL SOCIETY OF CHEMISTRY

EDGE ARTICLE

View Article Online
View Journal

Cite this: DOI: 10.1039/d6sc00573j

All publication charges for this article have been paid for by the Royal Society of Chemistry

Core–wing modulated squaraines with enhanced two-photon absorption and efficient photothermal eradication of bacteria

Xin-Ao Liu,[a] Xingtong Zhou,[a] Tong Zhang,[b] Congdi Shang,*[b] Liping Ding,*[a] Taihong Liu*[a] and Yu Fang[a]

Predictable structure–property relationships for near-infrared (NIR)-emitting chromophores and sustainable photothermal agents remain challenging. Herein, two series of indolenine-based squaraines are synthesized to investigate how core–wing structural modulation influences photophysical properties. Dicyanovinylene modification of the squaraine carbonyl core induces a substantial bathochromic shift and enriches de-activation pathways, while further wing functionalization strengthens intramolecular charge transfer (ICT) efficiency and enhances nonlinear two-photon absorption (2PA). Intrinsic zwitterionic stabilization and the bent-shaped molecular skeleton of bis(dicyanovinylene)-cored squaraines are also supported by theoretical calculations. Optimal benzindolenine-winged squaraine dye SQ2-4CN demonstrates a strong two-photon absorption cross-section (δ_{2PA}) of 2140 GM at 890 nm within the NIR biological spectral window, approximately 8.95-fold enhancement over that of the indolenine-winged counterpart SQ1-2O. Femtosecond transient absorption spectroscopies further reveal the ICT character and plausible excited-state dynamics. Moreover, efficient bio-staining capability and photothermal eradication of bacteria with a significant photothermal conversion efficiency of 42.4% under 808 nm laser irradiation are initially validated for SQ2-4CN. The present work opens a pathway for designing core/wing-modified squaraines with superior nonlinear optical properties for potential bioimaging and photothermal applications.

Received 21st January 2026
Accepted 6th April 2026

DOI: 10.1039/d6sc00573j

rsc.li/chemical-science

Introduction

Bioimaging-guided photothermal therapy and diagnosis, enabling accurate and effective biological functionalities, have witnessed rapid development recently.[1] Intrinsic photophysical properties of chromophores and photothermal agents determine the bioimaging signal-to-noise ratio and therapeutic outcome efficacy.[2] Near-infrared (NIR)-emitting chromophores have attracted extensive attention in terms of deep tissue penetration depth, minimal photobleaching, low background noise, and multiplexed characteristics.[3] Among various NIR-emitting chromophores, squaraines (SQs) are characterized by intense and sharp absorption bands with high molar extinction coefficients ($\varepsilon > 10^5$ M^{-1} cm^{-1}), excellent photostability, and strong two-photon absorption (2PA).[4] They can be classified as symmetrical and asymmetrical analogues. Symmetrical ones are typically derived from the nucleophilic 1,3-dicondensation of electron-donating aromatics or heterocycles and squaric acid (3,4-dihydroxy-3-cyclobutene-1,2-dione), resulting in donor–acceptor–donor (D–A–D) type structural motifs.[5] However, the pronounced aggregation tendency of conventional SQs often leads to aggregation-caused quenching and diminished luminescence, calling for rational molecular design to mitigate these drawbacks.[6] Following the design strategies of π-conjugation extension and D–π–A strengthening, abundant nucleophilic heterocycle substituents have endowed versatile molecular variations of functional SQs and afforded favorable optical features.[7] In contrast to the extensively studied terminal modifications of electron-donating wings, squaraine core modification, which involves replacing the carbonyl oxygens with sulfur, mono-amino, mono-dicyanomethylene, or bis-dicyanomethylene groups, remains less explored (Fig. 1a).[8] Generally, stronger electron-donating wing substituents lead to more pronounced intramolecular charge transfer (ICT) and a narrower energy gap in the investigated SQs. Concurrently, the larger and more rigid the core modification, the greater the bent degree of the squaraine skeleton.[4a,9] Lambert *et al.* synthesized a series of mono(dicyanovinylene)-cored indolenine SQs with a stereogenic center in close proximity and revealed a twisted geometry for the phenyl-substituted cisoid squaraine

[a]Key Laboratory of Applied Surface and Colloid Chemistry of Ministry of Education, Shaanxi Provincial Key Laboratory of New Concept Sensors and Molecular Materials, School of Chemistry and Chemical Engineering, Shaanxi Normal University, Xi'an 710119, P. R. China. E-mail: liuth121@snnu.edu.cn; dinglp33@snnu.edu.cn

[b]College of Food Science and Engineering, Northwest A&F University, Yangling 712100, Shaanxi, P. R. China. E-mail: shangcd@nwafu.edu.cn

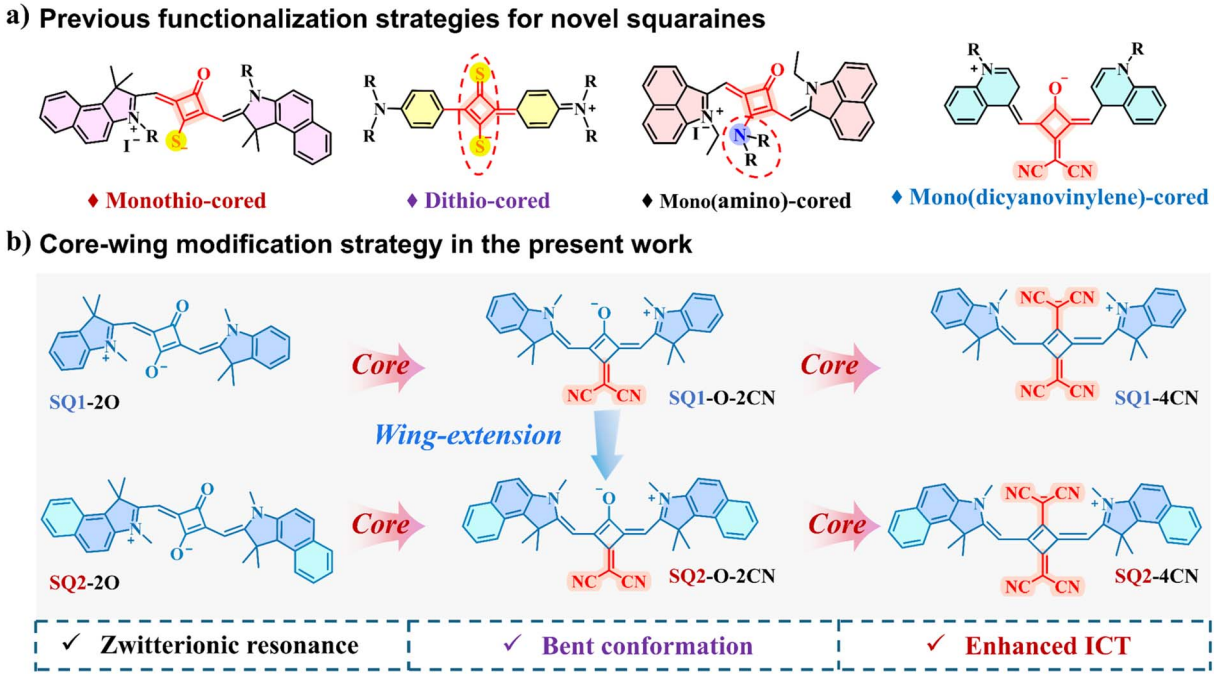

Fig. 1 (a) Previous core modification strategies for designing novel SQs. (b) Schematic core–wing modification strategy and molecular structures of the indolenine-winged SQ1 and benzindolenine-winged SQ2 series.

derivative.[10] In contrast, bulky bis-dicyanovinylene modifications can introduce significant steric hindrance, promoting profound symmetry breaking, twisted or bent ICT pathways.[10,11] Resultant charge transfer will regulate the corresponding fluorescence lifetime and quantum yield. Competitive non-radiative decays are desirable for the promising photothermal conversion.[12] Therefore, systematic core–wing modification and molecular architecture variations of the SQs constitute attractive motivations in pursuing optimal NIR-emitting and photothermal agents.

In this work, two series of indolenine-winged SQs (denoted as the SQ1 series) and benzindolenine-winged SQs (SQ2 series) are synthesized *via* a core–wing modification strategy (Fig. 1b). Within each series, the main structural difference lies in the core. The marked influence of these structural variations on steady-state optical properties is comprehensively examined. Core modification with the mono/bis(dicyanovinylene) group is found to alter the molecular symmetry from *trans*-conformation for the conventional SQs to *cis*-conformation for the dicyanovinylene-cored ones. Theoretical calculations further rationalize the resultant bent-shaped molecular skeleton, bent ICT, and high transition dipole moments. Degenerate 2PA properties are characterized using the open-aperture Z-scan technique and agree well with the accepted understanding of ICT and parity selection rules. Femtosecond transient absorption spectra (fs-TA) reveal that ICT, zwitterionic stabilization, and the bent-shaped skeleton promote non-radiative decays. The bioimaging functionality of representative SQ2-4CN is evaluated properly using an onion epidermal cell model, and further photothermal eradication of bacteria with a favorable photothermal conversion efficiency of the SQ2 series is investigated under 808 nm NIR laser excitation. These findings demonstrate potential biological and photothermal applications of the NIR-emitting core–wing modulated SQs.

Results and discussion

Synthesis and characterization of the two series of SQs

The indolenine-winged SQ1 dyes, especially the bis(dicyanovinylene)-cored counterpart SQ1-4CN, are obtained following reported procedures (Scheme S1).[6b,13] For the SQ2 series, conventional cyclobutene-cored dye SQ2-2O is synthesized *via* 1,3-dicondensation of squaric acid and 1,2,3,3-tetramethyl-1*H*-benzo[*e*]indol-3-ium iodide (Scheme S2).[14] Benzindolenine is purposely introduced to extend π-conjugation *via* wing modifications. Similarly, the condensation reaction between the benzindolenine precursor and triethylammonium-3-(dicyanomethylene)-2-ethoxy-4-oxocyclobut-1-enolate affords mono(dicyanovinylene)-cored SQ2-O-2CN (Scheme S3). Further treatment of SQ2-2O with Lawesson's reagent converts the dye into a dithio-cored intermediate.[13a] The sulfur atom is converted to a thiomethyl ether using a methylating agent, and a subsequent malononitrile substitution under basic conditions yields the target bis(dicyanovinylene)-cored squaraine SQ2-4CN (Scheme S4). Both SQ1-4CN and SQ2-4CN dissolve well in common organic solvents including CH_2Cl_2, $CHCl_3$, toluene (TOL), and tetrahydrofuran (THF).[8c] Due to the coplanar π-conjugation and quadrupolar character, all the SQs possess zwitterionic structures with rapid charge redistribution and resonance interconversion.[6a,15] The ^{1}H NMR chemical shifts of the SQ1s are comparatively investigated, focusing on the protons residing in

the five-membered indolenine ring (Fig. S1). The $C(CH_3)_2$ proton signals exhibit a progressive upfield shift following the trend of SQ1-2O (1.75 ppm) ≈ SQ1-O-2CN (1.73 ppm) > SQ1-4CN (1.52 ppm). Conversely, the *N*-methyl proton signals shift downfield to 3.59 ppm for SQ1-2O, 3.61 ppm for SQ1-O-2CN, and 3.87 ppm for SQ1-4CN, respectively. We can speculate that these chemical shifts are apparently associated with molecular configurations. Planar SQ1-2O and SQ1-O-2CN account for the proximity of NMR signals, whereas non-planar and bent-shaped SQ1-4CN results in distinct spin–spin splitting and intensity integration.[10]

Linear optical properties of the SQs

To elucidate the structure–property relationships of the SQs with varied core–wing modifications, their steady-state absorption and fluorescence emission are initially characterized in $CHCl_3$. Initially, the parent dye SQ2-2O exhibits an absorption maximum at 663 nm with a ε value of 2.81×10^5 M^{-1} cm^{-1} and a small full width at half maximum (FWHM) of 27 nm (Fig. 2a, S2a and d). These spectral features are consistent with an intense π–π* transition and can be assigned as the transition from the ground state (S_0) to the first singlet excited state (S_1) (Fig. 2a and S2a).[16] An additional short-wavelength band at around 378 nm is plausibly assigned to the $S_0 \rightarrow S_2$ (the second singlet excited state) transition.[12a] Interestingly, *cis*-conformational SQ2-O-2CN shows a red-shifted absorption peak at 711 nm ($\varepsilon = 2.74 \times 10^5$ M^{-1} cm^{-1}), accompanied by a higher-energy $S_0 \rightarrow S_2$ transition at 401 nm (Fig. 2a, S2b and e).[12a,17] Further bis(dicyanovinylene)-cored SQ2-4CN results in a significantly bathochromic absorption maximum at 765 nm (Fig. 2a and S2c). Its markedly decreased ε value of 7.20×10^4 M^{-1} cm^{-1} and a much broader spectral profile with a FWHM of 82 nm can be attributed to a bent-shaped molecular skeleton, which disrupts the delocalized π-conjugation and ICT character related to the core substitution (Fig. S2f).[17] Concomitantly, the $S_0 \rightarrow S_2$ transition red-shifts to a longer wavelength shoulder at 481 nm (Fig. 2a). It should be emphasized that one more band at 342 nm is specially assigned to the $S_0 \rightarrow S_3$ (the third singlet excited state) transition (Fig. 2a and S2c). The optical bandgaps

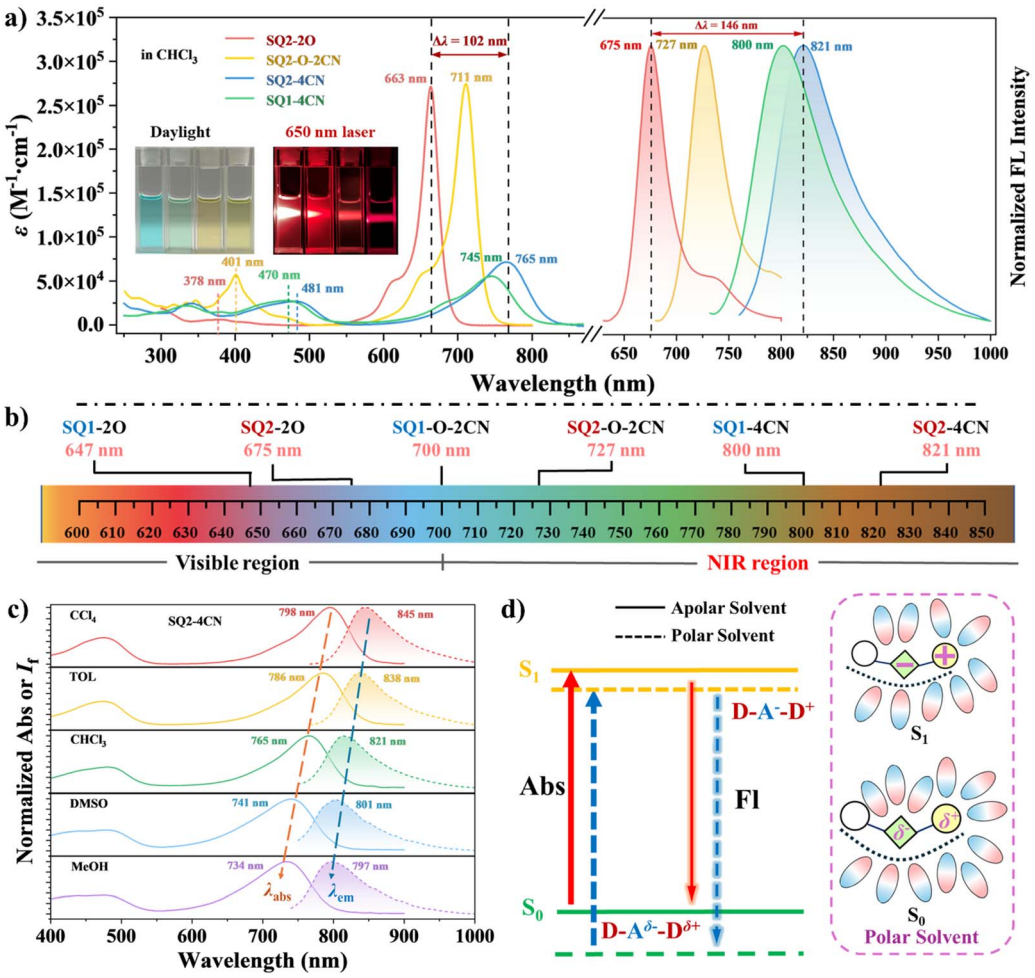

Fig. 2 (a) Comparative UV-vis absorption and fluorescence emission spectra of the SQ2 series and the control dye SQ1-4CN in dilute $CHCl_3$. Insets show the solution colors of the SQs (from left to right: SQ2-2O, SQ2-O-2CN, SQ2-4CN, and SQ1-4CN) under daylight and 650 nm laser light (~10^{-5} M). (b) Fluorescence peak distribution of the investigated SQs in $CHCl_3$. (c) Normalized absorption (solid lines) and emission (dashed lines) spectra of SQ2-4CN in different organic solvents. (d) Plausible effect of solvent polarity on the photoexcitation processes of SQ2-4CN.

Table 1 Summarized photophysical properties of the two investigated squaraine series

Dyes[a]	λ_{abs} (nm)	ε (M^{-1} cm^{-1})	λ_{em} (nm)	$\Delta\lambda/\Delta\tilde{\nu}$ (nm cm^{-1})	FWHM (nm)	Φ_F	E_g^{opt}[b] (eV)	τ (ns)	μ_{01}[c] (D)	λ_{2PA} (nm)	δ_{2PA} (GM)
SQ2-2O	663	2.81×10^5	675	12/268	27	23.8%	1.805	2.61	12.32	730	1920
SQ2-O-2CN	711	2.74×10^5	727	16/309	34	20.8%	1.685	3.84	13.49	—	—
SQ2-4CN	765	7.20×10^4	821	56/892	82	3.5%	1.514	1.68	9.26	890	2140
SQ1-4CN	745	5.59×10^4	800	55/923	87	7.2%	1.550	3.31	8.53	850	1730

[a] In dilute $CHCl_3$. [b] E_g^{opt} (eV) $= 1240/\lambda_{edg}$. [c] $\mu_{01} = 0.09584 \times \sqrt{\int \frac{\varepsilon(\nu)}{\nu^{max}} d\nu}$

(E_g^{opt}) of the SQ2 series are narrowed from 1.805 eV for SQ2-2O to 1.514 eV for SQ2-4CN (Fig. S3). Comparatively, the analogue SQ1-4CN, featuring a less π-conjugated indolenine wing, exhibits similar spectral features except for the systematically blue-shifted absorption maximum at 745 nm. Meanwhile, its E_g^{opt} value of 1.550 eV is slightly larger than that of SQ2-4CN, supporting the incorporation of the less conjugated wing in the SQ1 series (Fig. 2a and S3). The transition dipole moments (μ_{01}) from the S_0 state to the excited S_1 state are determined as 8.53 D for SQ1-4CN and 9.26 D for SQ2-4CN in $CHCl_3$, respectively (Table 1).[18] Considering the dependence of 2PA efficiency on the μ_{01} values and detuning energy, the bis(dicyanovinylene)-cored SQs should be potential two-photon-absorbing chromophores.[19] Furthermore, bent-shaped SQ1-4CN and SQ2-4CN display pronounced negative solvatochromism, suggesting permanent dipole moments in the ground state and anti-intuitive electron density redistribution upon photoexcitation (Fig. S4–S6 and Table S1).[11c,20] A charge-separated ground-state behavior for the quadrupolar SQs is rationalized properly (Fig. 2c). This indicates that the pronounced charge-separation characteristics and bent molecular configuration in the ground state facilitate substantial stabilization by polar solvent molecules, resulting in significant energy lowering.

Upon photoexcitation, SQ2-2O in $CHCl_3$ exhibits an emission maximum at 675 nm along with a moderate fluorescence quantum yield (Φ_F) of 23.8%. Mono(dicyanovinylene)-cored SQ2-O-2CN displays a red-shifted emission at 727 nm, accompanied by a slightly decreased Φ_F value of 20.8% (Fig. 2a and b). In contrast, bis(dicyanovinylene)-cored SQ2-4CN shows a more pronounced bathochromic emission maximum reaching 821 nm. The Φ_F value of SQ2-4CN significantly reduces to 3.5% (Fig. 2b and Table 1).[15] We can speculate that sequential core modifications induce a systematic emission red-shift and enhance the ICT character. SQ2-4CN exhibits a markedly larger Stokes shift ($\Delta\lambda = 56$ nm/$\Delta\tilde{\nu} = 892$ cm^{-1}), reflecting structural relaxation that directly contributes to its predominant non-radiative decay (Table S1). The average fluorescence lifetime increases from 2.61 ns for SQ2-2O to 3.84 ns for SQ2-O-2CN, then decreases slightly to 1.68 ns for SQ2-4CN (Fig. S7). This non-monotonic trend can be rationalized by the excessively small energy gap resulting from enhanced charge separation.[21] The mono/bis(dicyanovinylene)-core modification may facilitate radiative transitions in different trends. The solution colors of the SQ2 series vary from dark blue (CIE 0.646, 0.327) for SQ2-2O to olive green (CIE 0.197, 0.169) for SQ2-4CN under daylight, and show apparent fluorescence changes under 650 nm laser light (Fig. 2a and S8). A similar trend is observed in the SQ1 series, validating the consistent structure–property correlation of the core modification (Table S2). It is noteworthy that the emission maxima of bis(dicyanovinylene)-cored SQs exhibit anomalous blue-shifts, indicating a larger ground-state dipole moment than that of the excited state (Fig. 2c and S9).[22] The D–A–D structure of SQ2-4CN permits an excited-state structural bending that decreases its polarity, resulting in a larger ground-state dipole moment—a reversal of the trend observed in planar squaraines (Fig. 2d).

Optimized structures and theoretical calculations of the SQs

To clarify the influence of core modifications on the geometries and optical transitions, theoretical calculations of the investigated SQs are conducted systematically based on the density functional theory (DFT) at the CAM-B3LYP/6-311G(d,p) level in vacuum. As reported previously, planar SQ2-2O arranges in a *trans*-conformation,[23] and mono(dicyanovinylene)-cored SQ2-O-2CN features a *cis*-conformation with a C_{2v} symmetry (Fig. S10).[10,13a] Further core functionalization with the second dicyanovinylene group induces accentuated skeleton bending.[10] *cis*-Conformational SQ2-4CN with a C_1 symmetry adopts a bent-shaped coplanar degree of 170.48° between the adjacent carbon atoms. Furthermore, the benzindolenine planes are slightly twisted out of plane, possessing a dihedral angle of 27.55° between the central ring and benzindolenine wings (Fig. 3a). A similar bent-shaped molecular skeleton with a bent degree of 170.73° and twisted dihedral angle of 26.91° is found in SQ1-4CN (Fig. S11). Electrostatic potential (ESP) analysis reveals that the positively charged regions predominantly localize over the terminal wing units, while the electron-rich areas concentrate on the squaraine core (Fig. 3b). Moreover, the ground-state dipole moments of three core-substituted SQs are evaluated to elucidate the extent of intramolecular charge separation between positive and negative centers. Owing to the strong electron-withdrawing character of the dicyanovinylene core, SQ2-O-2CN displays a substantial ground-state dipole moment of 7.36 D, which is slightly smaller than that of 9.38 D for SQ2-4CN (Fig. 3b). The favorable value of SQ2-4CN is higher than that of 8.98 D for SQ1-4CN because of the D–A strengthening

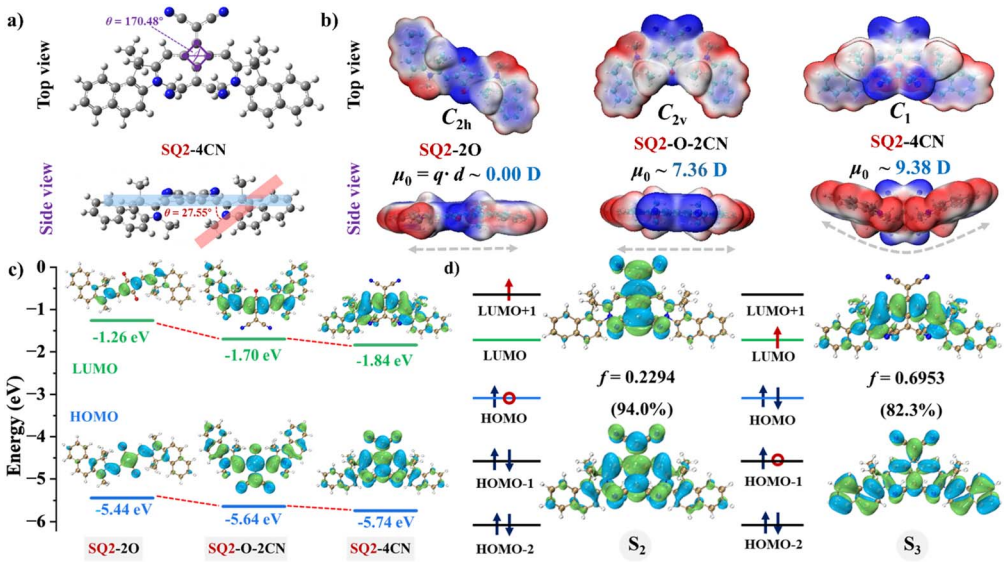

Fig. 3 (a) Optimized geometries and dihedral angles of the dye SQ2-4CN in their ground states. (b) ESP mapped and molecular dipoles of the SQ2 series. (c) Frontier molecular orbitals and energies level from the DFT calculations of the SQ2 series. (d) High-order absorption band orbital transition contributions in SQ2-4CN.

(Fig. 3b and S12). It demonstrates that the bis(dicyanovinylene)-cored SQ2-4CN exhibits a more pronounced zwitterionic contribution from the resonance structures, indicating a higher degree of charge separation.[17]

To gain deeper insights into the excited-state properties, the frontier molecular orbitals of the core-substituted SQs are systematically analyzed (Fig. 3c and S13). The HOMO and LUMO energy levels of the parent SQ2-2O are −5.44 eV and −1.26 eV, respectively. In contrast, the HOMO level of SQ2-O-2CN decreases to −5.64 eV, and the corresponding orbital is localized on the dicyanovinylene substituent and four-membered squaraine core, while the LUMO orbital of SQ2-O-2CN is predominantly delocalized across the central ring and terminal wing units, and the energy level also decreases to −1.70 eV (Fig. 3c). Similarly, the two energy levels of SQ2-4CN decrease to −5.74 eV and −1.84 eV, respectively. An obvious decreasing trend is also found in the SQ1 series (Fig. S13). It can be inferred that dicyanovinylation core modification lowers the energy levels and narrows the energy gaps, which is consistent with the red-shifted steady-state parameters (Table 1). Due to the significant reduction in molecular symmetry induced by dicyanovinylene substitution, all the dicyanovinylene-substituted SQs exhibit the basic $S_0 \rightarrow S_1$ transition and higher-order absorption bands, for example, transitions from the S_0 state to the S_2 state ($S_0 \rightarrow S_2$) and the S_0 state to the S_3 state ($S_0 \rightarrow S_3$) (Fig. 3d, S14, S15 and Table S3). Taking SQ2-4CN as an example, its $S_0 \rightarrow S_2$ transition is mainly contributed by the theoretical HOMO → LUMO+1 transition (94.0%, f = 0.2294). And the $S_0 \rightarrow S_3$ transition is contributed by the HOMO−1 → LUMO excitation (82.3%, f = 0.6953) (Fig. 3d).[24]

Nonlinear 2PA properties of the SQs

Two-photon-absorbing chromophores have gained extensive attention for practical applications such as two-photon excited fluorescence microscopy, optical power limiting, three-dimensional microfabrication, optical data storage, *etc.*[4c,6a,25] Degenerate 2PA properties of both squaraine series are evaluated over the 700–1000 nm spectral range using the typical open-aperture Z-scan technique.[26] All the investigated SQs exhibit characteristic reverse saturable absorption (RSA) behavior, showing decreased transmission at the focus (Fig. 4a and S16).[25,27] SQ2-4CN features strong δ_{2PA} values of 365–2140 GM (GM ≡ 10^{-50} cm^4 s per photon per molecule) in the spectral region of 880–1000 nm, which falls well in the NIR biological spectral window (Table S4).[28] Accordingly, it exhibits a corresponding 2PA cross-section (δ_{2PA}) maximum of 2140 GM at 890 nm (Fig. 4b, c and Table S4). On one hand, the 2PA wavelength maxima shift progressively from 730 nm of SQ2-2O to 890 nm of SQ2-4CN (Fig. S17 and Table S5). A similar red-shifted trend of the 2PA wavelength maxima is observed in the SQ1 series, from 710 nm (1240 GM) of SQ1-2O to 850 nm (1730 GM) of SQ1-4CN (Fig. 4b, S18, Tables S6 and S7). On the other hand, extended π-conjugation and a strengthened D–A–D character promote greater electron delocalization and consequently improve the 2PA efficiency. Considering a weak δ_{2PA} value of 239 GM for SQ1-2O at 890 nm, an 8.95-fold enhancement is observed for the core–wing modified SQs (Fig. S18 and Table S6).[12a]

A four-level model is employed to illustrate the transition pathways (Fig. 4d). The strong 2PA peak at 730 nm for the centrosymmetric SQ2-2O corresponds to the one-photon absorption (1PA) forbidden $S_0 \rightarrow S_2$ transition (λ = 378 nm), adhering to the parity selection rule of gerade → gerade (g → g).[18] In contrast, noncentrosymmetric SQ2-4CN exhibits a 2PA maximum at 890 nm, a nearly 2-fold wavelength correlation with the 1PA shoulder around 481 nm of SQ2-4CN (Fig. 4c).[5c,22,29] Additionally, the transmission rates at the focus decreased with increasing laser intensities, and the constant δ_{2PA} and 2PA

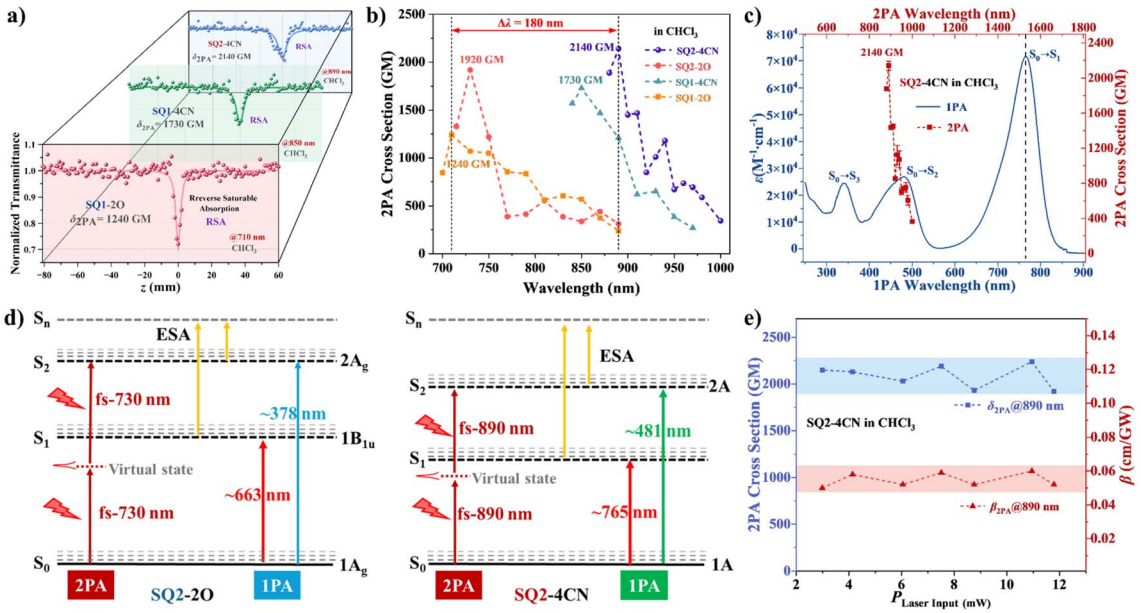

Fig. 4 (a) Normalized transmittance curves and δ_{2PA} values of SQ1-2O, SQ1-4CN, and SQ2-4CN in $CHCl_3$. (b) Degenerate δ_{2PA} values of the SQs ranging from 700 to 1000 nm under different excitation wavelengths. (c) Combined 1PA and 2PA spectra of SQ2-4CN in$CHCl_3$. (d) Compared state energies diagram of the 1PA/2PA processes for SQ2-2O and SQ2-4CN. (e) Diagram of measured δ_{2PA} and β values at fs-890 nm *versus* input laser power at the focal plane.

coefficient (β) values support the prominent 2PA contribution (Fig. 4e and S19).[19] Similarly, SQ1-4CN shows a δ_{2PA} maximum of 1730 GM at 850 nm, following the parity selection rules according to the 1PA shoulder peak at 470 nm (Fig. S18b and Table S7). We can conclude that the 2PA mechanism of SQs is closely related to their molecular configuration, and both the 2PA efficiency and wavelength maxima are jointly regulated by the core structure and conjugated wing architectures.

Excited-state dynamics revealed by femtosecond transient absorption (fs-TA) spectroscopies

fs-TA is an important method to study the photoinduction kinetics of conjugated chromophores and explore their photophysical processes. Upon excitation at 750 nm, SQ2-4CN in $CHCl_3$ exhibits a ground-state bleaching (GSB) signal centered at 765 nm, which aligns well with its steady-state UV-vis absorption maximum (Fig. 5a and S20). A concurrent stimulated emission (SE) band simultaneously emerges around 820 nm, indicating a rapid population of the S_1 state. As the GSB and SE signals decay, a broad positive excited-state absorption (ESA) band concomitantly grows featuring a maximum around 580 nm within the spectral region of 500–650 nm. A distinct isosbestic point around 675 nm suggests interconversion between the excited-state species (Fig. 5a). The influence of core modifications on excited-state behaviors and dynamics is systematically investigated. The ESA maxima occur at 560 nm for SQ2-2O and 558 nm for the mono(dicyanovinylene)-cored SQ2-O-2CN with relatively high excited-state energies (Fig. 5b, S21 and S22). Interestingly, SQ2-2O and SQ1-2O exhibit distinct ESA signals within 800–900 nm, typically assigned to transitions from the lowest ICT excited states (S_1) to higher excited states (S_n) (Fig. 5b and S23–25).[15] However, for the bis(dicyanovinylene)-cored SQ2-4CN and SQ1-4CN, no obvious ESA peak is found in the long-wavelength spectral region (Fig. 5a and S26). Corresponding ESA lifetimes of 1591.6 ps for SQ2-2O increase to 1980.8 ps for SQ2-O-2CN and decrease markedly to 541.1 ps for SQ2-4CN, and fully corroborate with the fluorescence lifetime measurements (Fig. S27). Further global and multi-wavelength fitting of the transient data enables resolving the excited-state dynamics (Fig. 5c and S28). The spectral evolution of D–A–D type SQ2-4CN can be described by three distinct transient species. Upon photoexcitation, charge-separated SQ2-4CN in the ground state ($D–A^{\delta-}–D^{\delta+}$) rapidly populates into the Franck–Condon (FC) state. Within 4.4 ps, it evolves rapidly into the excited state *via* solvent and structural relaxation. Subsequently, SQ2-4CN overcomes a substantial CT energy barrier *via* a rearrangement of the D–A–D framework, and evolves over 113.3 ps into the less polar [$D–A^{-}–D^{+}$]* state with more pronounced charge separation. Finally, it recombines to the S_0 state with a lifetime of 537.8 ps (Fig. 5c and S28).

To test this hypothesis, we subsequently investigate the differences in the excited-state behavior of conventional SQ1-2O and SQ2-4CN in solvents of varying polarity. SQ2-4CN shows ESA peaks at 584 nm (TOL), 580 nm ($CHCl_3$), and 588 nm (DMSO), demonstrating minimal solvatochromic effect (Fig. 5d).[30] It is noteworthy that the GSB/SE signal peak of SQ1-2O exhibits a red-shift from 650 nm in TOL to 658 nm in DMSO. Conversely, the corresponding signal peak of SQ2-4CN shows a blue-shift from 801 nm in TOL to 788 nm in DMSO (Fig. 5d and S29–31). While for SQ2-4CN, polar solvents preferentially stabilize its highly polar ground state, resulting in anomalous

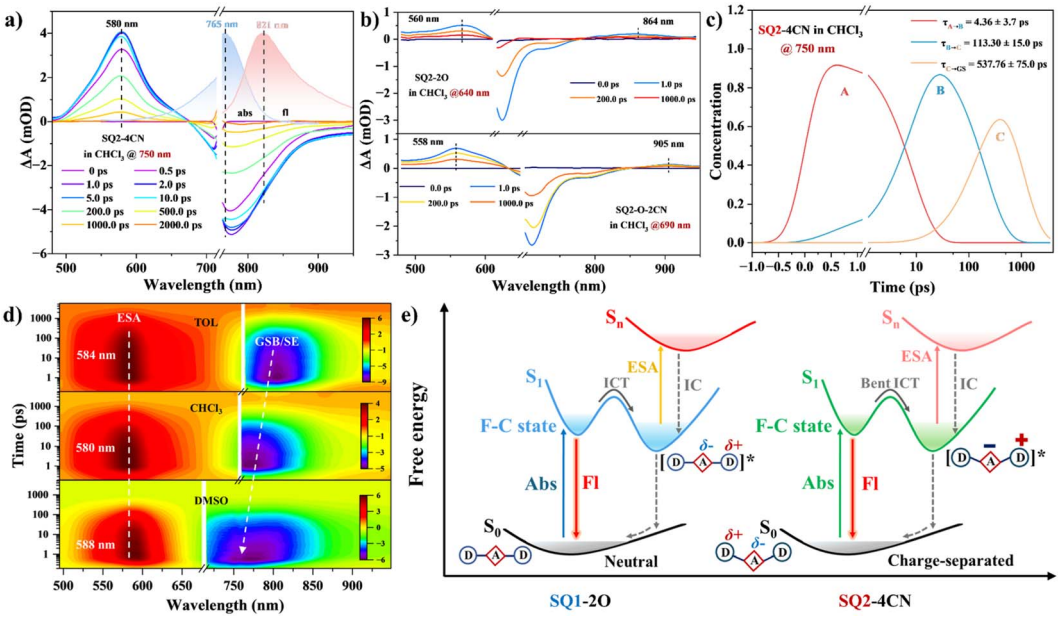

Fig. 5 (a) fs-TA delay spectra of SQ2-4CN excited at fs-750 nm in $CHCl_3$, the blue and red shaded regions represent steady-state absorption and emission spectra. (b) fs-TA delay spectra of SQ2-2O and SQ2-O-2CN in $CHCl_3$. (c) Species-associated spectra plots of SQ2-4CN in $CHCl_3$ excited at fs-750 nm. (d) Related 2D contour map of the fs-TA spectra of SQ2-4CN in TOL, $CHCl_3$, and DMSO. (e) Comparative impact of molecular configuration on the photoexcitation process of SQ1-2O and SQ2-4CN.

emission blue-shifts with increasing solvent polarity. The CT process in the SQs can be rapidly stabilized through dipole–dipole interactions in polar solvents, which is manifested by the shortening of ESA lifetimes. The ESA lifetime of planar SQ1-2O shortens from 1528.3 ps in TOL to 571.7 ps in DMSO. In contrast, the ESA lifetime of bent SQ2-4CN reduces from 952.4 ps in TOL to 182.9 ps in DMSO, corresponding to a significant enhancement in the CT rate (Fig. S32 and Table S8). These experimental results verify that SQ2-4CN undergoes a bent ICT process, which is characterized by a reduction in the excited-state dipole moment and a concomitant enhancement in the degree of charge separation (Fig. 5e).

Plant fluorescence imaging and photothermal conversion studies

Aiming to achieve the proof-of-concept objectives, cellular experiments with the SQs were first conducted utilizing onion epidermal cells as a model. SQ2-4CN exhibits bright red fluorescence upon excitation at 630 nm and shows significant fluorescence enhancement within the cellular environment (Fig. 6a). It shows high affinity toward the lignin-rich regions of the cell wall, and the cell wall thickness is averaged to be approximately 7.8 μm (Fig. 6b).[4c] We know that photothermal therapy is a promising strategy for physically destroying microorganisms with minimum toxic effects. Based on the extended absorption wavelength and pivotal non-radiative pathways, SQ2-4CN might facilitate efficient photothermal conversion and convert the absorbed light into heat.[31] Upon 808 nm laser irradiation at a power density of 1.5 W cm^{-2}, different temperature levels are achieved with increasing the illumination time. The temperature of SQ2-4CN in DMSO increases markedly from 20.1 °C to 61.2 °C within 10 min. In contrast, those values of SQ2-O-2CN and SQ2-2O only moderately rise to 30.2 °C and 24.6 °C, respectively (Fig. 6c). SQ2-4CN also demonstrates satisfactory photostability and thermal stability over four successive heating–cooling cycles (Fig. 6d). Considering the actual biological sample environment, we next assess the photothermal performance of SQ2-4CN in a DMSO/water (1/9, v/v) solution. SQ2-4CN is studied by real-time monitoring of temperature changes at various concentrations under different laser power densities. The data indicate that the photothermal effect of SQ2-4CN is dependent on both power density and concentration (Fig. S33). Based on the cooling time and the corresponding negative natural logarithm of the dimensionless driving force temperature $-\ln(\theta)$, the associated heat transfer time constant (τ_s) is determined as 3.598 min (Fig. 6e).[30] And the photothermal conversion efficiency (η) of the system is calculated to be approximately 42.4% (Fig. 6e and S34). In the context of the growing challenge of antibiotic resistance, the development of novel antibacterial strategies based on near-infrared photothermal agents holds significant research importance and application value. The antibacterial activities of SQ2s against *E. coli* with and without NIR laser illumination are further investigated by the plate count method (Fig. 6f and S35). An incremental temperature increase causes irreversible tissue injury to the bacteria, activating the coagulative necrosis process and leading to bacterial eradication.[32] SQ2-4CN exhibits excellent antibacterial activity against *E. coli*, with the antibacterial efficiency reaching approximately 94% under 808 nm laser irradiation (Fig. 6g). The survival rate of *E. coli* in the presence of SQ2-4CN ($c \sim 10^{-3}$ M) increases to ~70% (Fig. 6g), exhibiting certain dark toxicity of the investigated SQ2-

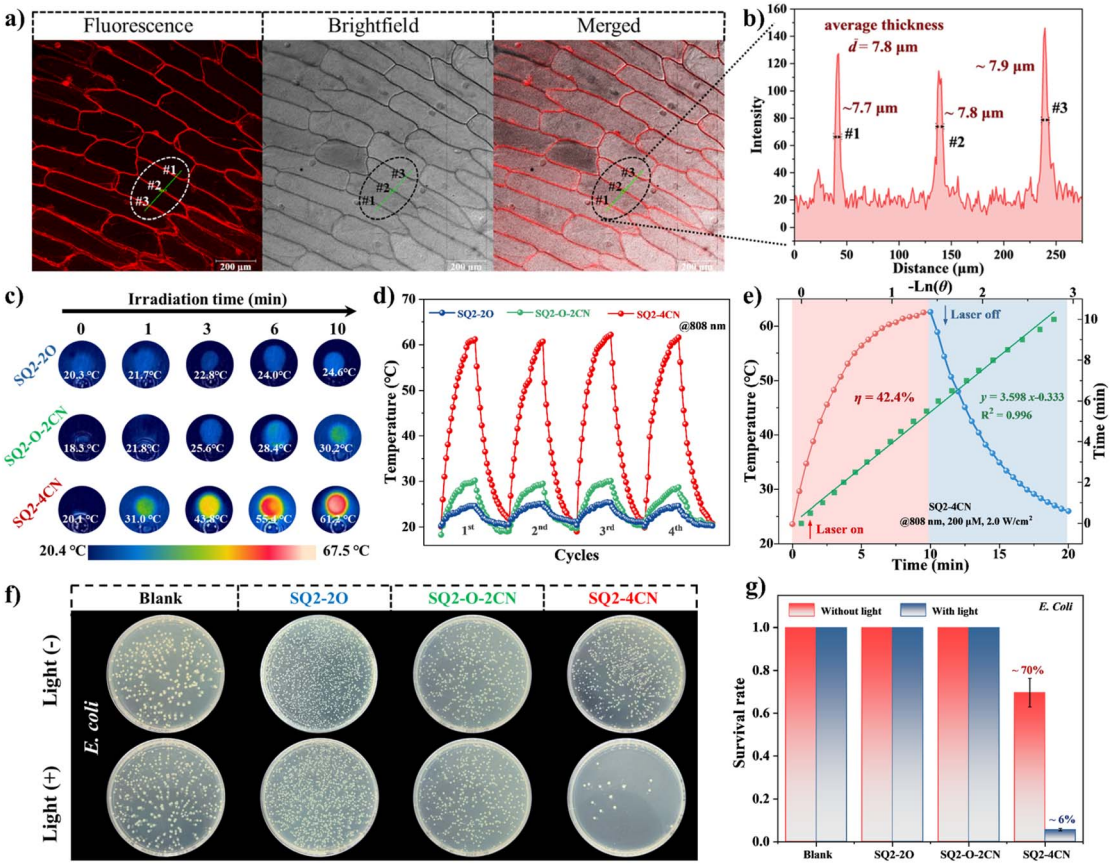

Fig. 6 (a) CLSM images of the onion epidermal cells incubated with SQ2-4CN. (b) Spectral intensity analyses of the onion epidermal cells stained with SQ2-4CN. (c) Infrared thermographs of the SQ2 series in a DMSO solution (10^{-3} M, 1.0 mL) under laser irradiation at various time points. (d) Temperature elevation of the SQ2 series (10^{-3} M) in DMSO under four irradiation/cooling cycles (808 nm laser, 1.5 W cm^{-2}, 10 min). (e) Temperature rise/fall curves and the cooling time *vs.* $-\ln(\theta)$ plot. Notes: θ represents the driving force temperature for SQ2-4CN. (f) Comparative visualization effect on *E. coli* colonies in the presence of the SQ2s series with and without 808 nm laser irradiation. (g) Survival rate of *E. coli* cultured with SQ2s under 808 nm laser irradiation. Error bars are calculated from independent experiments ($n = 3$).

4CN.[33] We also observed negligible antibacterial activity for the analogues SQ2-2O and SQ2-O-2CN under the same irradiation conditions (Fig. 6g and S35), underscoring the potential of bis(dicyanovinylene)-cored SQs as photothermal agents.

Conclusions

In this work, we synthesize two series of SQs with systematic core–wing modifications to investigate their intrinsic structure–property relationships. As the squaraine core is progressively substituted with dicyanovinylene groups, pronounced red-shifts in both UV-vis absorption and fluorescence emission are observed. Higher-order absorption bands and strong ICT are rationalized in the bis(dicyanovinylene)-cored SQs, accompanied by significant non-radiative decay rates and a bent-shaped molecular skeleton. Notably, bis(dicyanovinylene)-cored and benzindolenine-winged SQ2-4CN possesses a large δ_{2PA} value of 2140 GM at 890 nm, attributed to its high transition dipole moment, small detuning energy, and symmetry-induced parity selection rules. Theoretical calculations highlight that the bent molecular geometry and enhanced ICT are key factors governing both the steady-state optical parameters and 2PA efficiency. Ultrafast TA results manifest the distinct excited-state dynamics and the correlation of solvent-dependent behaviors with the core/wing modifications. SQ2-4CN demonstrates favorable bioimaging functionalities and a high photothermal conversion efficiency of 42.4% under 808 nm laser irradiation, highlighting its promising antibacterial activity through photothermal ablation. These findings offer critical insights into the rational design of multifunctional SQs.

Author contributions

The manuscript is written through contributions of all authors. X.-A. Liu performed most of the experimental work and data analyses and wrote the original draft. X. Zhou and T. Zhang participated in the data analysis. C. Shang and T. Liu supervised the experimental work, analyzed the data, and revised the manuscript. L. Ding and Y. Fang supervised the project and revised the manuscript.

Conflicts of interest

There are no conflicts to declare.

Data availability

The data supporting this article have been included in the main text and the supplementary information (SI). Supplementary information is available. See DOI: https://doi.org/10.1039/d6sc00573j.

Acknowledgements

The authors acknowledge funding from the National Natural Science Foundation of China (22572113 and 22172097), the National Key Research and Development Program of China (2022YFA1205502), and the Shaanxi Provincial Science Fund for Distinguished Young Scholars (2025JC-JCQN-044).

References

1 (*a*) S. Yuan, J. Zhou, J. Wang, X. Ma, F. Liu, S. Chen, J.-X. Fan and G.-P. Yan, *Mol. Pharmaceutics*, 2024, **21**, 467–480; (*b*) S. Xu, K.-C. Yan, Z.-H. Xu, Y. Wang and T. D. James, *Chem. Soc. Rev.*, 2024, **53**, 7590–7631.

2 (*a*) J. Kim, Y. Xu, J. H. Lim, J. Y. Lee, M. Li, J. M. Fox, M. Vendrell and J. S. Kim, *J. Am. Chem. Soc.*, 2025, **147**, 701–712; (*b*) W. Liu, C. Lv, Y. Hou, X. Lou, Z. Ma, M. He, X. Zeng, W. Sun, J. Fan and X. Peng, *Sci. China: Chem.*, 2025, **68**, 5065–5073; (*c*) V.-N. Nguyen, Z. Zhao, B. Z. Tang and J. Yoon, *Chem. Soc. Rev.*, 2022, **51**, 3324–3340.

3 (*a*) Z. Zhang, A. Mei, W. Wang, K. Xu, M. Wang, P. Chen, J. Shao and X. Dong, *Coord. Chem. Rev.*, 2025, **545**, 217026; (*b*) L. Xu, Q. Zhang, X. Wang and W. Lin, *Coord. Chem. Rev.*, 2025, **543**, 216910; (*c*) L. He, Y. Li, C. Zhang, X. Zhang, B. Wang, T. Ren and L. Yuan, *Coord. Chem. Rev.*, 2025, **533**, 216549; (*d*) H. Li, Y. Kim, H. Jung, J. Y. Hyun and I. Shin, *Chem. Soc. Rev.*, 2022, **51**, 8957–9008.

4 (*a*) R. Song, Y. Dong, Z. Zhong, Q. Zhao, Y. Hu, M. Lei, P. Lei, Z. Jiang, K. Qian, C. Shi, Z. He, Y. Qin, J. Wang and H. Chen, *J. Med. Chem.*, 2024, **67**, 10275–10292; (*b*) A. Mei, X. He, D. Lei, L. Wang, W. Wang, J. Shao, Q. Shen, F. Jiang and X. Dong, *Coord. Chem. Rev.*, 2025, **527**, 216419; (*c*) N. Zhang, H. Chang, R. Miao, T. Liu, L. Ding and Y. Fang, *J. Mater. Chem. B*, 2024, **12**, 5350–5359.

5 (*a*) E. Lima, O. Ferreira, V. S. D. Gomes, A. O. Santos, R. E. Boto, J. R. Fernandes, P. Almeida, S. M. Silvestre and L. V. Reis, *Dyes Pigm.*, 2019, **167**, 98–108; (*b*) U. Mayerhöffer, B. Fimmel and F. Würthner, *Angew. Chem., Int. Ed.*, 2012, **51**, 164–167; (*c*) M. V. Bondar, S. Faryadras, N. Munera, H.-J. Chang, M. Uddin, K. D. Belfield, O. D. Kachkovsky, E. W. Van Stryland and D. J. Hagan, *J. Phys. Chem. B*, 2022, **126**, 3897–3907.

6 (*a*) T. Liu, X. Liu, W. Wang, Z. Luo, M. Liu, S. Zou, C. Sissa, A. Painelli, Y. Zhang, M. Vengris, M. V. Bondar, D. J. Hagan, E. W. Van Stryland, Y. Fang and K. D. Belfield, *J. Phys. Chem. C*, 2018, **122**, 3994–4008; (*b*) K. Ilina, W. M. MacCuaig, M. Laramie, J. N. Jeouty, L. R. McNally and M. Henary, *Bioconjugate Chem.*, 2020, **31**, 194–213.

7 (*a*) L. Si, J. Tang, K. Yang, M. Wang, Y. Wang, G. Xia and H. Wang, *Chem. Sci.*, 2025, **16**, 7077–7086; (*b*) L. E. McNamara, T. A. Rill, A. J. Huckaba, V. Ganeshraj, J. Gayton, R. A. Nelson, E. A. Sharpe, A. Dass, N. I. Hammer and J. H. Delcamp, *Chem.–Eur. J.*, 2017, **23**, 12494–12501; (*c*) H.-J. Chang, M. V. Bondar, T. Liu, X. Liu, S. Singh, K. D. Belfield, A. Sheely, A. E. Masunov, D. J. Hagan and E. W. Van Stryland, *ACS Omega*, 2019, **4**, 14669–14679.

8 (*a*) S. F. Völker and C. Lambert, *Chem. Mater.*, 2012, **24**, 2541–2553; (*b*) C.-A. Shen, M. Stolte, J. H. Kim, A. Rausch and F. Würthner, *J. Am. Chem. Soc.*, 2021, **143**, 11946–11950; (*c*) C.-A. Shen and F. Würthner, *Chem. Commun.*, 2020, **56**, 9878–9881; (*d*) B. Jin, X. Zhang, W. Zheng, X. Liu, J. Zhou, N. Zhang, F. Wang and D. Shangguan, *Anal. Chem.*, 2014, **86**, 7063–7070; (*e*) H. Ye, L. Cui, T. Matsushima, C. Qin and C. Adachi, *ACS Appl. Mater. Interfaces*, 2018, **10**, 27–31; (*f*) J. Wu, D. Yang, Q. Wang, L. Yang, H. Sasabe, T. Sano, J. Kido, Z. Lu and Y. Huang, *J. Mater. Chem. A*, 2018, **6**, 5797–5806; (*g*) U. Mayerhöffer, M. Gsänger, M. Stolte, B. Fimmel and F. Würthner, *Chem.–Eur. J.*, 2013, **19**, 218–232; (*h*) S. R. Pristash, K. L. Corp, E. J. Rabe and C. W. Schlenker, *ACS Appl. Energy Mater.*, 2020, **3**, 19–28; (*i*) J. Liu, B. Zhao, X. Zhang, D. Guan, K. Sun, Y. Zhang and Q. Liu, *Angew. Chem., Int. Ed.*, 2024, **63**, e202316192.

9 (*a*) G. H. Rao, P. J. S. Rana, R. K. Chitumalla, J. Jang and S. P. Singh, *ACS Omega*, 2018, **3**, 15416–15425; (*b*) Y. Aydogan-Sun, A. Egyed, A. H. Winter and J. Wachtveitl, *J. Am. Chem. Soc.*, 2025, **147**, 28002–28014.

10 J. Selby, M. Holzapfel, B. K. Lombe, D. Schmidt, A.-M. Krause, F. Würthner, G. Bringmann and C. Lambert, *J. Org. Chem.*, 2020, **85**, 12227–12242.

11 (*a*) H. Moon, Q. P. Xuan, D. Kim, Y. Kim, J. W. Park, C. H. Lee, H.-J. Kim, A. Kawamata, S. Y. Park and K. H. Ahn, *Cryst. Growth Des.*, 2014, **14**, 6613–6619; (*b*) M. A. Kochman, *J. Phys. Chem. A*, 2024, **128**, 6685–6694; (*c*) F. Terenziani, O. V. Przhonska, S. Webster, L. A. Padilha, Y. L. Slominsky, I. G. Davydenko, A. O. Gerasov, Y. P. Kovtun, M. P. Shandura, A. D. Kachkovski, D. J. Hagan, E. W. Van Stryland and A. Painelli, *J. Phys. Chem. Lett.*, 2010, **1**, 1800–1804.

12 (*a*) C.-L. Sun, S.-K. Lv, Y.-P. Liu, Q. Liao, H.-L. Zhang, H. Fu and J. Yao, *J. Mater. Chem. C*, 2017, **5**, 1224–1230; (*b*) X. Xia, C. Shi, S. He, R. Wang, Z. Zhang, Y. Hu, J. Cao, T. Liu, D. Zhou, W. Sun, J. Fan and X. Peng, *Adv. Funct. Mater.*, 2023, **33**, 2300340.

13 (*a*) V. V. Kurdyukov, I. V. Kurdyukova, S. V. Shishkina and I. S. Konovalova, *J. Mol. Struct.*, 2023, **1271**, 134038; (*b*) Y. Liu, Q.-Y. Zhao, A. Li, Y. Zheng, Y. Gao, X.-F. Wang, Y. Kawai, T. Nakamura and S.-i. Sasaki, *J. Mater. Chem. A*, 2025, **13**, 10991–11002.

14 (*a*) Y. Uehashi, S. Izawa, Y. Yamada, Y. Miwa, T. Inuzuka, Y. Kubota, M. Hiramoto and K. Funabiki, *ChemistrySelect*, 2023, **8**, e202300309; (*b*) A. R. Ballestas-Barrientos, A. W. Woodward, W. V. Moreshead, M. V. Bondar and K. D. Belfield, *J. Phys. Chem. C*, 2016, **120**, 7829–7838.

15 N. Zhang, L. Liu, H. Chang, K. Liu, T. Liu, L. Ding and Y. Fang, *J. Phys. Chem. Lett.*, 2023, **14**, 7283–7289.

16 T. Liu, X. Liu, Y. Zhang, M. V. Bondar, Y. Fang and K. D. Belfield, *Eur. J. Org Chem.*, 2018, **2018**, 4095–4102.
17 A. L. Puyad, G. Krishna Chaitanya, A. Thomas, M. Paramasivam and K. Bhanuprakash, *J. Phys. Org. Chem.*, 2013, **26**, 37–46.
18 T. Liu, M. V. Bondar, K. D. Belfield, D. Anderson, A. E. Masunov, D. J. Hagan and E. W. Van Stryland, *J. Phys. Chem. C*, 2016, **120**, 11099–11110.
19 J. Zang, W. Feng, X. Chang, K. Liu, H. Peng, L. Ding, T. Liu and Y. Fang, *Dyes Pigm.*, 2021, **193**, 109487.
20 (*a*) K. M. Shafeekh, S. Das, C. Sissa and A. Painelli, *J. Phys. Chem. B*, 2013, **117**, 8536–8546; (*b*) F. Terenziani, A. Painelli, C. Katan, M. Charlot and M. Blanchard-Desce, *J. Am. Chem. Soc.*, 2006, **128**, 15742–15755.
21 Y. Li, J. Ye, Y. Li, M. Jing, T. Shi, H. Qiu and S. Yin, *Polym. Chem.*, 2023, **14**, 3008.
22 C. Benitez-Martin, J. M. Marin-Beloqui, J. T. L. Navarrete, J. Casado, F. Najera and E. Perez-Inestrosa, *Adv. Mater.*, 2025, e10730.
23 T. Maeda, S. Mineta, H. Fujiwara, H. Nakao, S. Yagi and H. Nakazumi, *J. Mater. Chem. A*, 2013, **1**, 1303–1309.
24 C.-L. Sun, Q. Liao, T. Li, J. Li, J.-Q. Jiang, Z.-Z. Xu, X.-D. Wang, R. Shen, D.-C. Bai, Q. Wang, S.-X. Zhang, H.-B. Fu and H.-L. Zhang, *Chem. Sci.*, 2015, **6**, 761–769.
25 W. Feng, K. Liu, J. Zang, G. Wang, R. Miao, L. Ding, T. Liu, J. Kong and Y. Fang, *ACS Appl. Mater. Interfaces*, 2021, **13**, 28985–28995.
26 W. Zhou, X. Wu, J. Xu, J. Li, J. Yang, Y. Wang, X. Zhang, J. Xiao and Y. Song, *Dyes Pigm.*, 2024, **225**, 112058.
27 W. Feng, K. Liu, J. Zang, J. Xu, H. Peng, L. Ding, T. Liu and Y. Fang, *J. Phys. Chem. B*, 2021, **125**, 11540–11547.
28 V. J. Pansare, S. Hejazi, W. J. Faenza and R. K. Prud'homme, *Chem. Mater.*, 2012, **24**, 812–827.
29 Y. Chen, W. Luo, K. Liu, T. Liu, L. Ding and Y. Fang, *Chin. J. Struct. Chem.*, 2025, **44**, 100704.
30 H. Chang, J. Feng, X.-A. Liu, R. Miao, T. Liu, L. Ding and Y. Fang, *Chem. Sci.*, 2025, **16**, 7424–7432.
31 (*a*) J. Yuan, H. Yang, W. Huang, S. Liu, H. Zhang, X. Zhang and X. Peng, *Chem. Soc. Rev.*, 2025, **54**, 341–366; (*b*) S. Cai, L. Wu, Y. Li, S. Samanta, J. Wang, B. Liu, F. Wu, K. Lai, Y. Liu, J. Qu and Z. Yang, *Chin. Chem. Lett.*, 2024, **35**, 108599.
32 M. Omidiyan, M. Wang, P. Tajalli, X. He, S. Hoijang, C. Cai, N. Chiang and T. R. Lee, *ACS Appl. Mater. Interfaces*, 2025, **17**, 64065–64076.
33 D. G. Ozburun, H. Hancer, B. Findikli, T. Ozbek, M. M. Ozmen and M. Topuzogullari, *Eur. Polym. J.*, 2025, **222**, 113615.